

# Nitroxide-Based Macromolecular Contrast Agents with Unprecedented Transverse Relaxivity and Stability for Magnetic Resonance Imaging of Tumors

Hung V.-T. Nguyen,<sup>†</sup> Qixian Chen,<sup>†</sup> Joseph T. Paletta,<sup>‡</sup> Peter Harvey,<sup>||</sup> Yivan Jiang,<sup>†</sup> Hui Zhang,<sup>‡</sup> Michael D. Boska,<sup>§,||</sup> M. Francesca Ottaviani,<sup>∇</sup> Alan Jasanoff,<sup>||,⊥,#</sup> Andrzej Rajca,<sup>‡</sup> and Jeremiah A. Johnson<sup>\*,†</sup>

<sup>†</sup>Department of Chemistry, <sup>||</sup>Department of Biological Engineering, <sup>⊥</sup>Department of Brain and Cognitive Sciences, and <sup>#</sup>Department of Nuclear Science and Engineering, Massachusetts Institute of Technology, 77 Massachusetts Avenue, Cambridge, Massachusetts 02139, United States

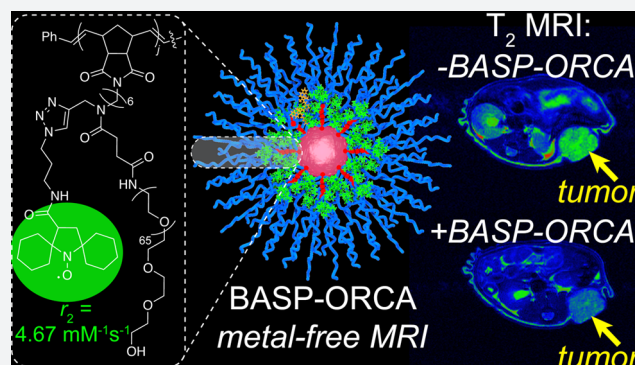
<sup>§</sup>Department of Radiology, University of Nebraska Medical Center, Omaha, Nebraska 68198, United States

<sup>∇</sup>Department of Pure and Applied Sciences, University of Urbino, Urbino 61029, Italy

<sup>‡</sup>Department of Chemistry, University of Nebraska, Lincoln, Nebraska 68588, United States

## S Supporting Information

**ABSTRACT:** Metal-free magnetic resonance imaging (MRI) agents could overcome the established toxicity associated with metal-based agents in some patient populations and enable new modes of functional MRI *in vivo*. Herein, we report nitroxide-functionalized brush-arm star polymer organic radical contrast agents (BASP-ORCAs) that overcome the low contrast and poor *in vivo* stability associated with nitroxide-based MRI contrast agents. As a consequence of their unique nano-architectures, BASP-ORCAs possess per-nitroxide transverse relaxivities up to ~44-fold greater than common nitroxides, exceptional stability in highly reducing environments, and low toxicity. These features combine to provide for accumulation of a sufficient concentration of BASP-ORCA in murine subcutaneous tumors up to 20 h following systemic administration such that MRI contrast on par with metal-based agents is observed. BASP-ORCAs are, to our knowledge, the first nitroxide MRI contrast agents capable of tumor imaging over long time periods using clinical high-field <sup>1</sup>H MRI techniques.



## INTRODUCTION

Among the many imaging modalities for medical diagnostics, magnetic resonance imaging (MRI) is one of the most useful thanks to its ability to noninvasively generate three-dimensional detailed anatomical images with high spatial resolution while not requiring an ionizing source and remaining insensitive to depth.<sup>1–4</sup> Current clinical MRI methods depict the spatial distribution and chemical environment of water protons (<sup>1</sup>H) within a region of interest (ROI); to enhance the differences between native water <sup>1</sup>H and ROIs, contrast agents are often employed. These contrast agents are divided into two primary classes: *T*<sub>1</sub> contrast agents (e.g., paramagnetic metals such as gadolinium or manganese) that afford positive-contrast images primarily by locally reducing the water <sup>1</sup>H longitudinal relaxation time (spin–lattice, *T*<sub>1</sub>), and *T*<sub>2</sub> contrast agents (e.g., superparamagnetic iron oxide nanoparticles) that afford negative-contrast images by locally reducing the water <sup>1</sup>H transverse relaxation time (spin–spin, *T*<sub>2</sub>).<sup>5,6</sup> The corresponding water <sup>1</sup>H relaxivities (*r*<sub>1</sub> and *r*<sub>2</sub>, respectively) of a contrast

agent characterize the extent to which the agent decreases the *T*<sub>1</sub> and *T*<sub>2</sub> times of water <sup>1</sup>H. Contrast agents with greater *r*<sub>1</sub> and *r*<sub>2</sub> values provide increased image contrast compared to those with lower values at the same concentration.<sup>6,7</sup>

Most MRI contrast agents with large *r*<sub>1</sub> and/or *r*<sub>2</sub> values contain metals that possess several unpaired electrons. For example, small molecule<sup>8–13</sup> and nanoparticle-based<sup>14–21</sup> contrast agents featuring Gd, Mn, Fe-oxide, and other metals have been reported to function as either *T*<sub>1</sub> or *T*<sub>2</sub> contrast agents or both. Furthermore, metal-based contrast agents that display advanced functions such as multimodal imaging,<sup>8–10,12,13,17,20,21</sup> enhanced target-specific accumulation,<sup>14,18,19</sup> and/or sensing<sup>8,11–14</sup> have been developed. Despite their unquestionable utility, metal-based contrast agents, especially nanoparticle ones that tend to accumulate in biological tissues, may present toxicity concerns in some

Received: June 14, 2017

Published: July 12, 2017

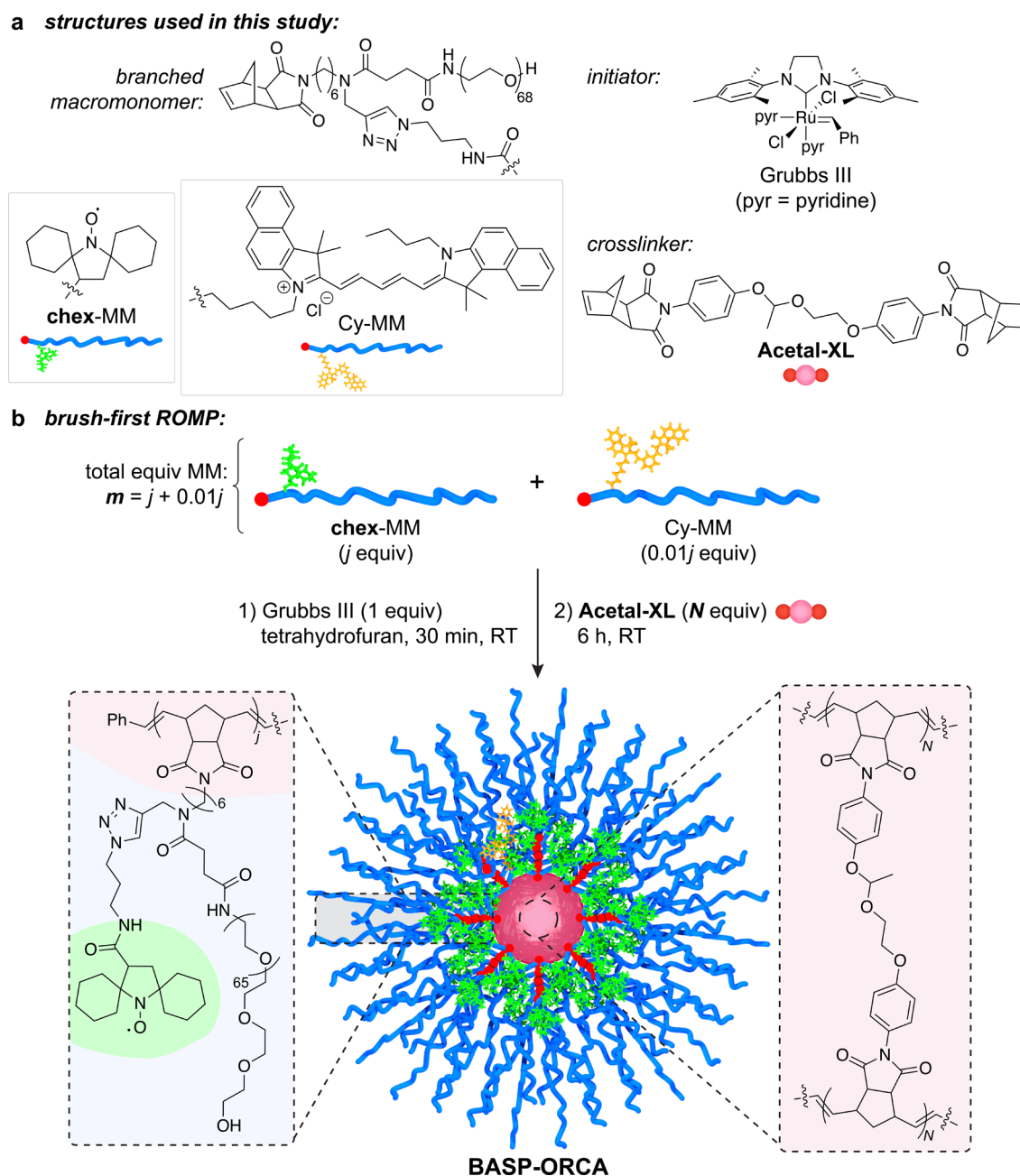


**Figure 1.** (a) Chemical structures of BASP components studied in this work. (b) General brush-first ROMP procedure. Branched MMs **chex-MM** and **Cy-MM** are combined in the ratio  $j : 0.01j$ . This combination of MMs is exposed to 1.0 equiv of Grubbs III initiator to produce a living bottlebrush with an average degree of polymerization (DP) =  $j + 0.01j = m$ .  $N$  equiv of **acetal-XL** is then added (in aliquots of 5 equiv of **acetal-XL** every 5 min) to provide the final BASP-ORCA. The properties of the BASP-ORCAs are defined by their  $m$  and  $N$  values (Table 1).

patient populations. For example, Gd-based agents, perhaps the most widely used  $T_1$  contrast agents in the clinic, are associated with potentially lethal nephrogenic systemic fibrosis, and they have recently been linked to a rising prevalence of toxic Gd ions in the environment.<sup>5,22–28</sup> In addition, several  $T_2$  contrast agents based on Fe-nanoparticles have been stopped from further development or withdrawn from the market due to safety concerns.<sup>29–32</sup> Moreover, according to the FDA, Fe-based products including ferumoxytol (Feraheme), the only FDA-approved superparamagnetic iron oxide nanoparticle currently available on the market, carry a risk of potentially life-threatening allergic reactions.<sup>33–35</sup> Thus, there is extensive interest in the development of “metal-free” MRI contrast agents

that make use of entirely organic-based components. Such agents could enable MRI in at-risk patient populations, and they could potentially open new avenues for functional/responsive MRI based on *in vivo* organic transformations. Furthermore, organic nanoparticle contrast agents could provide safe alternatives in MR imaging applications that may require long-term tissue accumulation, such as tumor imaging.

Four main classes of metal-free MRI contrast agents have been the most widely studied: paramagnetic nitroxide-based organic radical contrast agents (ORCAs), hyperpolarized  $^{13}\text{C}$  agents,  $^{19}\text{F}$  MRI contrast agents, and chemical exchange saturation transfer (CEST) contrast agents. While  $^{19}\text{F}$  MRI and CEST agents have undergone many advances in recent

Table 1. Characterization Data for BASP-ORCAs and Control Compounds

| name                          | composition |          | diameter        |                            | relaxivity                          |                                     | notes                       |
|-------------------------------|-------------|----------|-----------------|----------------------------|-------------------------------------|-------------------------------------|-----------------------------|
|                               | <i>m</i>    | <i>N</i> | $D_h/\text{nm}$ | $D_{\text{TEM}}/\text{nm}$ | $r_1/\text{mM}^{-1} \text{ s}^{-1}$ | $r_2/\text{mM}^{-1} \text{ s}^{-1}$ |                             |
| 3-CP <sup>a</sup>             |             |          |                 |                            | 0.15                                | 0.17                                |                             |
| chex-MM <sup>b</sup>          |             |          |                 |                            | 0.21                                | 0.30                                |                             |
| chex-dendrimer <sup>a</sup>   |             |          |                 |                            | 0.44                                | 0.86                                |                             |
| chex-bottlebrush <sup>b</sup> | 55.55       |          | 17 <sup>b</sup> | n.d.                       | 0.32                                | 0.82                                |                             |
| BASP-ORCA                     | 5.05        | 20       | 31 ± 2          | n.d.                       | 0.27                                | 6.92                                | poor solubility (<10 mg/mL) |
| BASP-ORCA                     | 5.05        | 30       | 49 ± 6          | n.d.                       | 0.53                                | 7.11                                | poor solubility (<10 mg/mL) |
| BASP-ORCA1                    | 7.07        | 20       | 31 ± 4          | 37 ± 7                     | 0.41                                | 4.67                                | good solubility (>50 mg/mL) |
| BASP-ORCA                     | 7.07        | 30       | 36 ± 3          | n.d.                       | 0.35                                | 7.40                                | poor solubility (<10 mg/mL) |
| BASP-ORCA                     | 9.99        | 15       | 28 ± 3          | 38 ± 10                    | 0.33                                | 2.90                                | low relaxivity              |
| BASP-ORCA                     | 9.99        | 30       | 33 ± 4          | 39 ± 10                    | 0.37                                | 4.52                                | low relaxivity              |

<sup>a</sup>From refs 52 and 53. <sup>b</sup>From ref 80.

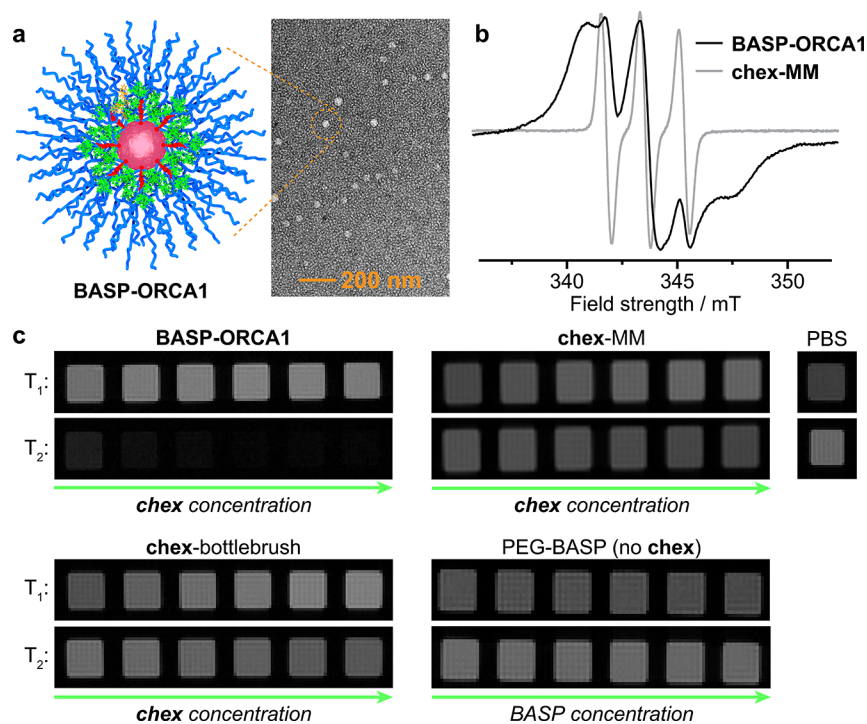


**Figure 2.** (a) Transmission electron microscopy image of BASP-ORCA1 ( $D_{\text{TEM}} = 37 \pm 7$  nm) after being negatively stained with uranyl acetate; the reported diameter ( $D_{\text{TEM}}$ ) represents the mean and standard deviation of >150 individual particle measurements. (b) Electron paramagnetic resonance (EPR) spectra for BASP-ORCA1 and chex-MM. (c)  $T_1$  and  $T_2$ -weighted MRI phantoms for BASP-ORCA1, chex-MM, PBS buffer, chex-bottlebrush, and a PEG-BASP lacking chex. The concentration of chex-containing samples (BASP-ORCA1, chex-MM, and chex-bottlebrush) ranges from 1 mM to 4 mM chex. The concentration of PEG-BASP lacking chex ranges from 6 mg/mL to 21 mg/mL, which is equivalent to the mass per volume concentration range of BASP-ORCA1.

years,<sup>36–43</sup> these approaches often suffer from low sensitivity, and in some cases, require a high contrast agent concentration (10–50 mM), long imaging times, and/or potentially harmful high-intensity radio frequency fields. Hyperpolarized <sup>13</sup>C agents, on the other hand, can theoretically afford up to 10<sup>5</sup> sensitivity improvements; nevertheless, issues including short hyperpolarization lifetimes that lead to limited imaging times, complexity in terms of the chemistry and instrumentation required for generation of the hyperpolarized agent, and a rather small substrate scope remain major challenges.<sup>44–46</sup> Furthermore, <sup>19</sup>F MRI, CEST, and hyperpolarized <sup>13</sup>C agents rely on imaging mechanisms that are not currently common in the clinic.<sup>44–51</sup> In contrast, nitroxide ORCAs rely on standard water relaxation mechanisms to achieve MRI contrast; they could in principle be immediately translated to clinical

applications. However, several key challenges limit the clinical feasibility of nitroxide ORCAs. First, nitroxide radicals only possess one unpaired electron. As a result, compared to metal-based contrast agents such as Gd<sup>3+</sup> (seven unpaired electrons) or Mn<sup>2+</sup> (five unpaired electrons), nitroxide ORCAs inherently suffer from much lower water <sup>1</sup>H relaxivity. One strategy to achieve higher molecular relaxivity is to use a poly(nitroxide) where the relatively low per nitroxide relaxivity is multiplied by the number of nitroxides bound to a polymer scaffold. The second major limitation of nitroxide ORCAs is that they are typically reduced rapidly *in vivo* (half-lives on the order of minutes) to diamagnetic hydroxylamines, thus rendering them ineffective as contrast agents shortly after injection.<sup>52–55</sup> Initial efforts to utilize nitroxides as MRI contrast agents exposed these shortcomings,<sup>56,57</sup> and though their rapid bioreduction

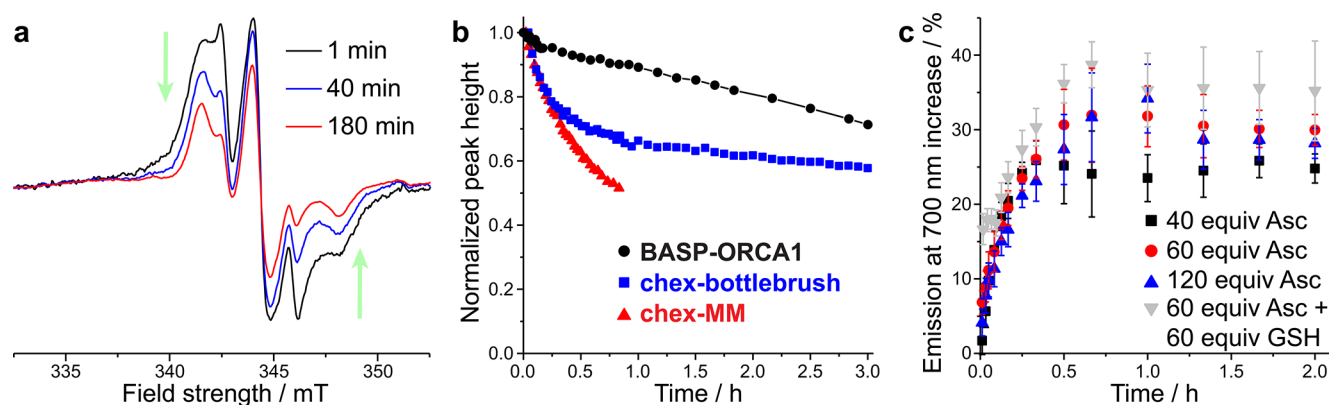


**Figure 3.** (a) EPR spectra for **BASP-ORCA1** 1, 40, and 180 min following exposure to 20 equiv of sodium ascorbate (Asc) per nitroxide. (b) Ascorbate reduction kinetics for **BASP-ORCA1**, **chex-bottlebrush**, and **chex-MM**. (c) Cy5.5 emission at 700 nm in response to Asc and glutathione (GSH); the reported values represent the mean and standard error of the mean (SEM) ( $n = 3$ ).

has been cleverly exploited to enable redox-mapping *in vitro* and *in vivo*,<sup>58–62</sup> an *in vivo*-stable nitroxide ORCA that allows for longitudinal studies over clinically meaningful time scales following systemic administration has yet to be developed.

Macromolecular nitroxide ORCAs with long-term *in vivo* stability could be particularly useful for tumor imaging. Nanoparticles of suitable size ( $\sim 10$ – $200$  nm) are known to passively accumulate in tumors, especially in murine models, via the enhanced permeation and retention effect, but hours to tens of hours are often needed to reach maximal accumulation.<sup>63–69</sup> To our knowledge, there are no nitroxide-based molecules or materials with demonstrated capability to provide *in vivo* MRI contrast after such long times. This problem is exacerbated in murine models where imaging is often used for preclinical studies of disease development: murine tissues contain higher levels of metabolic antioxidants, which lead to faster nitroxide reduction rates.<sup>70,71</sup> Thus, the development of stable nitroxide-based macromolecular ORCAs with high relaxivities could open a new arena of MRI applications, whereby the accumulation of contrast agents in diseased tissues could be monitored by MRI without off-site toxicity concerns.<sup>55,72,73</sup> Moreover, the synthetic versatility of polymeric materials could facilitate future image-guided drug delivery strategies.

Herein, we report the design, synthesis, and biological evaluation of a new class of nitroxide macromolecules—brush-arm star polymer ORCAs (**BASP-ORCAs**)—with unique structures that are designed to overcome the aforementioned challenges associated with tumor MRI with nitroxide-based contrast agents. **BASP-ORCAs** contain a high concentration of reduction-resistant nitroxide groups bound in an interlayer between a poly(ethylene glycol) (PEG) shell and a polyacetal core. Due to their shielded and dense nitroxide layer, yet hydrophilic PEGylated nanostructures, **BASP-ORCAs** simultaneously possess the highest known water  $^1\text{H}$  transverse relaxivities and stabilities for nitroxide ORCAs. In addition, the modularity of **BASP** synthesis was exploited to install near-infrared fluorophores into **BASP-ORCAs** and thereby achieve near-infrared fluorescence (NIRF) imaging in concert with MRI. Leveraging this combination of features, **BASP-ORCAs** were successfully employed for longitudinal MR and NIRF imaging of tumors with MRI contrast enhancement on par with metal-based contrast agents observed up to 1 day following systemic administration, which has, to our knowledge, never been achieved with a paramagnetic organic agent. Notably, though previous studies on nitroxide MRI contrast agents

focused on  $T_1$ -weighted imaging, **BASP-ORCAs** operate most effectively as  $T_2$  contrast agents, which is advantageous given that high-field instruments are being increasingly adopted in the clinic, and  $r_2$  often remains similar or increases with magnetic field strength.<sup>74</sup> Thus, **BASP-ORCAs** not only overcome the challenges that have plagued all previous nitroxide-based MRI contrast agents, and thereby facilitate the first longitudinal imaging of tumors with a nitroxide ORCA, but they are also naturally amenable to current and future clinical high-field MRI instruments.

## RESULTS AND DISCUSSION

**BASP-ORCA Design and Synthesis.** One of the most common ways to increase the relaxivity of MRI contrast agents

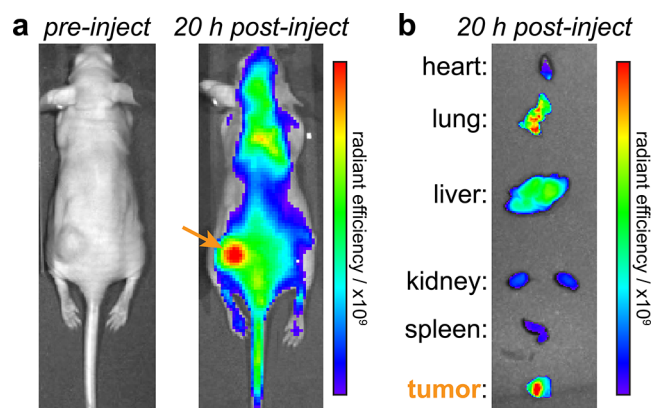


**Figure 4.** (a) *In vivo* NIRF images of NCR nude mouse before and 20 h after injection of **BASP-ORCA1** (see Supporting Information for details). (b) *Ex vivo* NIRF images of selected organs (see Supporting Information for details). Units of radiant efficiency:  $\frac{\text{p/sec/cm}^2/\text{sr}}{\mu\text{W/cm}^2}$ .

(including nitroxides) involves attaching them to a rigid macromolecular scaffold.<sup>6,47,52,53,75–78</sup> For example, Rajca and co-workers appended a spirocyclohexyl nitroxide derivative (“**chex**”)<sup>79</sup> to the surface of dendrimers to produce **chex**-dendrimer ORCAs where the per-**chex**  $r_1$  was  $0.42 \text{ mM}^{-1} \text{ s}^{-1}$  compared to  $r_1 = 0.14 \text{ mM}^{-1} \text{ s}^{-1}$  for the model nitroxide 3-carboxy-2,2,5,5-tetramethyl-1-pyrrolidinyloxy (3-CP).<sup>52,53</sup> In a later study, we appended **chex** to the core of PEGylated branched-bottlebrush polymers.<sup>80</sup> The resulting “**chex-bottlebrush**” had a per-**chex**  $r_1$  of  $0.32 \text{ mM}^{-1} \text{ s}^{-1}$ , which was

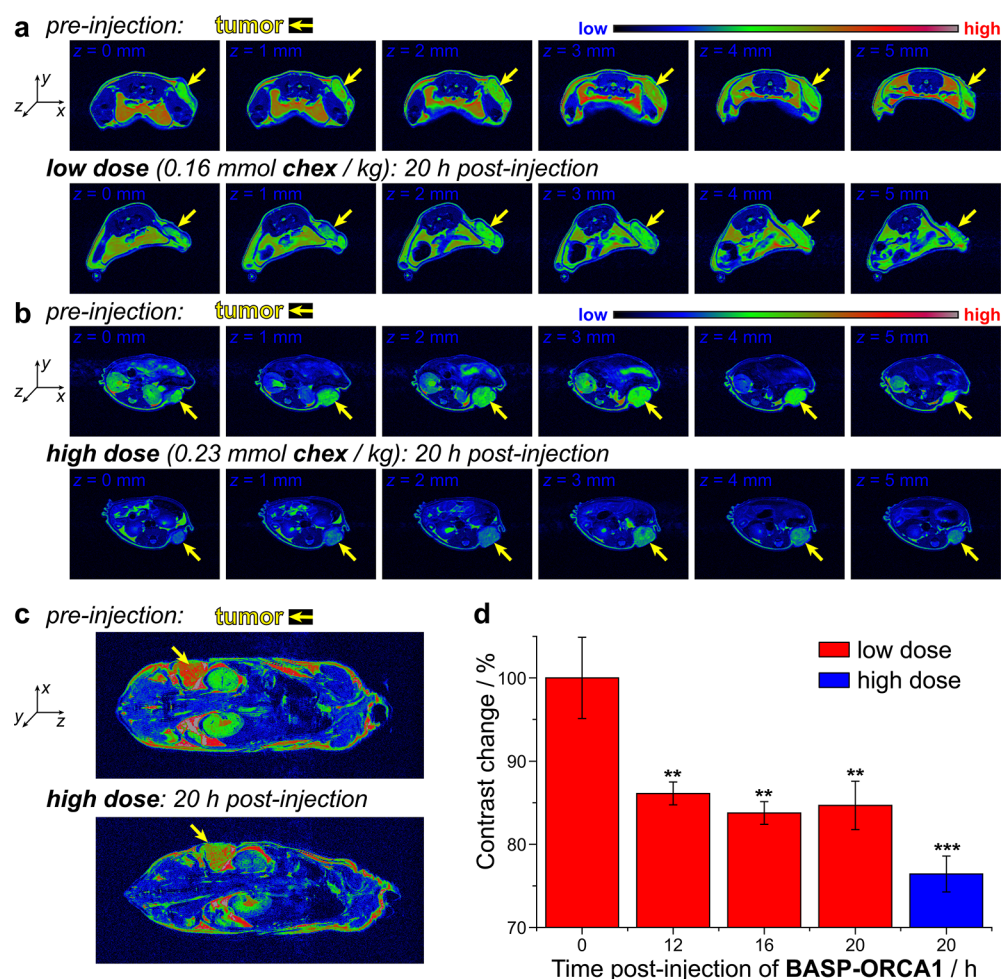


**Figure 5.** (a)  $T_2$ -weighted MR images of tumor bearing NCR nude mouse before (top row) and 20 h after (bottom row) injection of 0.16 mmol **chex**/kg (“low dose”) of **BASP-ORCA1**. Each series of images corresponds to progressive slices in the  $z$ -axis through the tumor of the same mouse. (b)  $T_2$ -weighted MR images of tumor bearing NCR nude mouse before (top row) and 20 h after (bottom row) injection of 0.23 mmol **chex**/kg (“high dose”) of **BASP-ORCA1**. Each series of images corresponds to progressive slices in the  $z$ -axis through the tumor of the same mouse. (c)  $T_2$ -weighted coronal MR images before (top) and 20 h after (bottom) injection of 0.23 mmol **chex**/kg (“high dose”) of **BASP-ORCA1**. (d) Percent MRI contrast change at various times following **BASP-ORCA1** injection compared to preinjection. Statistical comparisons ( $n = 3$  for low dose group;  $n = 4$  for high dose group; reported values represent mean  $\pm$  SEM) to preinjection images were made with a student  $t$  test: \*\* $P \leq 0.05$ , \*\*\* $P \leq 0.001$ .

approximately 50% greater than the **chex**-macromonomer used to synthesize these polymers (**chex-MM**, Figure 1a). In this system,  $r_2$  also increased from  $0.30 \text{ mM}^{-1} \text{ s}^{-1}$  for **chex-MM** to  $0.82 \text{ mM}^{-1} \text{ s}^{-1}$  for the **chex**-bottlebrush polymer, thus demonstrating that increasing the macromolecular size and **chex** density leads to increases in both  $r_1$  and  $r_2$ , with a greater increase in  $r_2$ .<sup>80</sup> In an effort to further increase these relaxivity values, we sought to incorporate **chex** into our **BASP** macromolecules wherein the nitroxides would be bound at a rigid core–shell interface.<sup>80–83</sup> On the basis of this novel structure compared to previous systems, we hypothesized that **BASPs** could provide enhanced relaxivity and nitroxide stability potentially making tumor imaging *in vivo* possible. Moreover, the control and robustness of **BASP** synthesis would enable the scalable production of **BASP-ORCAs** with optimal sizes for tumor accumulation, which is difficult with previous macromolecular systems such as dendrimers and bottlebrush polymers.<sup>84–86</sup>

**BASP-ORCAs** were synthesized by brush-first ring-opening metathesis polymerization (ROMP) as depicted in Figure 1.<sup>84,86–88</sup> Norbornene-based branched macromonomers (MMs,

Figure 1a) featuring 3 kDa PEG and either **chex** (**chex-MM**) or Cy5.5 dye (**Cy-MM**, Figure 1a) were copolymerized by exposure to Grubbs third-generation bis-pyridine initiator<sup>89</sup> (Grubbs III, Figure 1a; reaction stoichiometry:  $j$  equiv. **chex-MM** to  $0.01j$  **Cy-MM** to 1.0 Grubbs III) for 30 min (Figure 1b). The resulting living bottlebrush polymers with an average degree of polymerization (DP) of  $\sim j + 0.01j = m$  were then cross-linked via portionwise addition of  $N$  equiv of bis-norbornene acetal cross-linker **acetal-XL**<sup>84</sup> (Figure 1a) to the reaction mixture to generate the desired **BASP-ORCA** (Figure 1b). With this method, the **BASP-ORCA** size is determined by the MM to Grubbs III to **acetal-XL** ratios (i.e.,  $m$  and  $N$  values). Much less **Cy-MM** ( $0.01j$ ) relative to **chex-MM** ( $j$ ) was used to bridge the difference in concentration requirements between MRI (mM to  $\mu\text{M}$ ) and NIRF (nM to pM).<sup>1,6</sup>

To identify optimal conditions for the synthesis of **BASP-ORCAs** with narrow size distributions and average diameters of  $\sim 25$ – $40$  nm, as well as high water solubility and relaxivity, we screened  $m$  and  $N$  values from 5–10 and 15–30, respectively (Table 1). Gel permeation chromatography (GPC) revealed nearly quantitative MM-to-bottlebrush conversion as well as

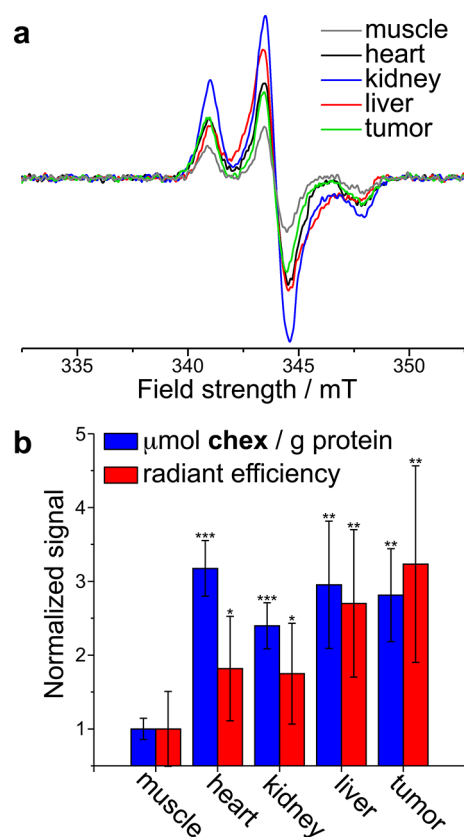


**Figure 6.** (a) EPR spectra obtained for homogenized tissue samples collected for the same mice imaged in Figure 5 22 h following **BASP-ORCA1** injection. (b) Blue: Muscle-normalized concentration of **chex** per gram of protein as obtained from EPR double integration of tissue homogenates. Red: Muscle-normalized concentration of Cy5.5 in tissue homogenates as obtained from NIRF imaging. Statistical comparisons ( $n = 4$ ; reported values represent mean  $\pm$  SEM) to muscle signal were made with a Student's  $t$  test: \*not significant, \*\* $P \leq 0.05$ , \*\*\* $P \leq 0.001$ .

$\geq 85\%$  bottlebrush-to-BASP conversion for all  $m$  and  $N$  values (Figure S1). The **BASP-ORCA** diameters as determined by dynamic light scattering (DLS) and transmission electron microscopy (TEM) ranged from  $\sim 28$  to  $\sim 49$  nm (Table 1). In general, for the same bottlebrush arm length ( $m$ ), the **BASP-ORCA** size increased with the amount of **acetal-XL** added ( $N$ ). In addition, the **BASP-ORCA** aqueous solubility (Table 1) increased with  $m$ . A representative TEM image for the  $m = 7.07$  and  $N = 20$  **BASP-ORCA** (referred to as **BASP-ORCA1** throughout the remainder of this work) is provided in Figure 2a. The aqueous solubility of **BASP-ORCA1** was the highest amongst the **BASP-ORCAs** prepared, and its hydrodynamic diameter ( $D_h$ ) of  $31 \pm 4$  nm is suitable for extended *in vivo* circulation and tumor accumulation.<sup>66–68</sup>

#### Characterization of **BASP-ORCA** Magnetic Properties.

Electron paramagnetic resonance spectroscopy (EPR) was used to confirm the presence of **chex** in **BASP-ORCAs**, as well as to study the **chex** environment in **BASP-ORCA1**. The spin concentrations were  $\geq 85\%$  for all **BASP-ORCAs**. The height-normalized EPR spectra for **BASP-ORCA1** and **chex-MM**<sup>80</sup> are shown in Figure 2b. The spectrum for **BASP-ORCA1** is significantly broader than **chex-MM**, which is consistent with the larger and more rigid **BASP** nanostructure where **chex** is bound at the dense interface between the acetal cross-linker core and the PEG shell (Figures 1b and 2b). The **BASP-**

**ORCA1** spectrum was simulated using the procedure developed by Budil, Freed, and co-workers<sup>90</sup> (see Supporting Information section A for details), which allows for characterization of the **chex** mobility in terms of the correlation time for rotational diffusion ( $\tau$ ). The spectrum was best fitted by superimposing two computed components (Figure S3): 22% corresponded to a relatively fast-moving nitroxide with  $\tau = 0.2$  ns, while 78% corresponded to a slow-moving nitroxide with  $\tau = 10.0$  ns. The faster-moving component likely corresponds to nitroxides that are furthest from the **BASP-ORCA1** acetal core (Figure 1b), while the slow-moving component corresponds to nitroxides that are close to and/or entangled within the acetal core. Notably, the  $\tau$  of 10.0 ns measured for the slow component in **BASP-ORCA1** is quite large, which suggests that a majority of the **chex** groups are in a rigid environment. For comparison, in our previously reported **chex-dendrimer ORCAs**,<sup>52,53</sup> **TEMPO-labeled bottlebrush polymers**,<sup>81,82</sup> and **BASPs**,<sup>83</sup> the largest  $\tau$  measured was  $\sim 1$  ns.

Next, we evaluated the longitudinal ( $r_1$ ) and transverse ( $r_2$ ) relaxivities of these **BASP-ORCAs** using a Bruker 7 T MRI scanner. The per-**chex**  $r_1$  values as a function of  $m$  and  $N$  (Table 1) ranged from 0.27 to 0.53  $\text{mM}^{-1} \text{s}^{-1}$ ; they were not significantly increased compared to Rajca's **chex-dendrimer** and our **chex-bottlebrush** polymers. However, the per-**chex**  $r_2$  values ranged from 2.90 to 7.40  $\text{mM}^{-1} \text{s}^{-1}$ , which is  $\sim 3.5$ - to  $\sim 9.0$ -fold greater than the per-**chex**  $r_2$  in our **chex-bottlebrush** polymers and  $\sim 17$ - to  $\sim 44$ -fold greater than **3-CP** (Table 1).<sup>80</sup> **BASP-ORCA1** displayed a per-**chex**  $r_2$  value of 4.67  $\text{mM}^{-1} \text{s}^{-1}$ . Though this value was not the highest we measured, we selected **BASP-ORCA1** for translation to biological studies because it offered the best balance of high relaxivity, solubility (greater than 50 mg/mL, Table 1), and size. Given the number-average molar mass of **BASP-ORCA1** as determined by gel permeation chromatography and static light scattering ( $M_n = 4.75 \times 10^5$  g/mol,  $D = 1.32$ ), we estimate that each **BASP-ORCA1** particle contains an average of 92 **chex** groups. Thus, the estimated average molecular  $r_1$  and  $r_2$  values for **BASP-ORCA1** are 37.6  $\text{mM}^{-1} \text{s}^{-1}$  and 428.8  $\text{mM}^{-1} \text{s}^{-1}$ , respectively, which are greater than those for the commonly used FDA-approved Gd-based contrast agent **Magnevist** ( $r_1 = 3.1 \text{mM}^{-1} \text{s}^{-1}$  and  $r_2 = 5.4 \text{mM}^{-1} \text{s}^{-1}$  at 7 T) and iron-based nanoparticles such as **Feraheme** ( $r_1 = 3.1 \text{mM}^{-1} \text{s}^{-1}$  and  $r_2 = 68 \text{mM}^{-1} \text{s}^{-1}$  at 7 T).<sup>91–94</sup>

MR phantom images of phosphate-buffered saline (PBS) solutions of **BASP-ORCA1**, **chex-MM**, and our previously reported **chex-bottlebrush** polymer at various **chex** concentrations (from 1 mM–4 mM **chex**) as well as a **PEG-BASP** that lacks **chex** (at equivalent mass fractions to **BASP-ORCA1**) are provided in (Figure 2c), along with images for “blank” PBS buffer. The  $T_1$ -weighted images for **BASP-ORCA1**, and **chex-bottlebrush** polymer are not obviously different, while the  $T_2$ -weighted images clearly show a large reduction in signal for **BASP-ORCA1**. The **PEG-BASP** with no **chex** shows no difference in contrast as a function of concentration, which confirms that **chex** is required to observe changes in image contrast.

The data presented above demonstrate that the high nitroxide density of **BASP-ORCA1**, which is a consequence of its unique cross-linked multilayer nanostructure, affords an increased magnetization capability that leads to  $r_2$  enhancement. This finding is consistent with reports where nitroxides are utilized as magnetic catalysts for outer-sphere relaxation processes.<sup>95–97</sup> Most importantly, the exceptionally high  $r_2$  of

**BASP-ORCA1** overcomes one of the major limitations of nitroxide-based contrast agents: inherently low contrast.

**Ascorbate Quenching Kinetics of BASP-ORCAs.** As discussed above, nitroxide-based ORCAs typically suffer from rapid reduction to diamagnetic hydroxylamines under biologically relevant conditions. Among the many potential biological reducing agents, ascorbate (Asc) is known to play a major role in *in vivo* nitroxide reduction,<sup>54,98,99</sup> and Asc-induced reduction can be amplified by glutathione (GSH).<sup>80,99</sup> We hypothesized that the rigid **chex** environment in our BASP-ORCAs could help to lower the rate of **chex** reduction. To test this hypothesis, we collected EPR spectra for **BASP-ORCA1** at various times following exposure to 20 equiv of Asc and 20 equiv of GSH per nitroxide (both reagents were present in 10 mM concentrations). EPR spectra collected 1, 40, and 180 min after exposure to these conditions are provided in Figure 3a. The changes in peak height as a function of time are indicative of nitroxide reduction. The normalized peak height of the EPR spectra are plotted versus time in Figure 3b. Reduction kinetics data for our previous **chex**-bottlebrush polymers and **chex-MM** are provided for comparison.<sup>80</sup> In contrast to the **chex**-bottlebrush and **chex-MM** samples, which both display an initial rapid **chex** reduction phase in the first hour, the reduction of **chex** in **BASP-ORCA1** was significantly retarded with nearly 85% remaining after 1 h, and 70% remaining after 3 h (compared to 65% and 57%, respectively, for the **chex**-bottlebrush). On the basis of the integrated peak heights as a function of time, the second-order rate constants for **BASP-ORCA1** reduction in the initial (first 10 min) and late (>1 h) stages of the reduction process were calculated:  $k_{\text{early}} = 0.0376 \text{ M}^{-1} \text{ s}^{-1}$  and  $k_{\text{late}} \approx 0.00672 \text{ M}^{-1} \text{ s}^{-1}$  (Table S1).<sup>52,53,80</sup> Simulations revealed that the EPR spectra collected during the reduction process consisted of a “fast” and a “slow” component (Figure S3). Interestingly,  $\tau$  for the “fast” component remained constant at 0.2 ns, while  $\tau$  for the “slow” component became increasingly larger with time (11.0 ns at 40 min and 13.2 ns at 180 min). Therefore, even after 3 h there persists an extremely reduction resistant and slow moving nitroxide population. The presence of these very stable nitroxides within **BASP-ORCA1** may enable T<sub>2</sub>-weighted MRI over longer time scales than have been possible with previous nitroxide contrast agents (*vide infra*).

**Fluorescence Properties of BASP-ORCAs.** As noted above, Cy5.5 was also incorporated into these BASP-ORCAs (see Figure S4 for **BASP-ORCA1** absorption and emission spectra confirming the presence of Cy5.5) in order to simultaneously use NIRF as an imaging modality for comparison to MRI. Nitroxides are well-known to quench fluorescence via catalysis of nonemissive photophysical processes such as intersystem crossing. This quenching requires close interaction between the nitroxide and the fluorophore; the systems with the greatest quenching typically feature the nitroxide directly linked to the fluorophore via  $\pi$  bonds (i.e., electronic conjugation).<sup>100–102</sup> Given the fact that **chex** and Cy5.5 are incorporated into BASP-ORCAs via two different macromonomers and that the mobility of **chex** is limited in these constructs, we reasoned that Cy5.5 quenching would be minimal; therefore, we could potentially use Cy5.5 emission as a fairly constant descriptor of particle concentration regardless of the extent of **chex** reduction.

To test this hypothesis, we exposed **BASP-ORCA1** to a large excess of Asc (40–120 equiv. to **chex**) in water, and monitored the resulting Cy5.5 emission. In agreement with our expect-

ation, only a  $25 \pm 2\%$  to  $30 \pm 2\%$  increase in fluorescence emission was observed (Figure 3c). Moreover, addition of GSH (60 equiv) as a coreductant along with 60 equiv of Asc gave only a  $35 \pm 7\%$  increase in fluorescence. Taken together, these data suggest that Cy5.5 fluorescence is minimally quenched by **chex** in **BASP-ORCA1**. For comparison, exposure of our previously reported **chex**-bottlebrush polymer containing Cy5.5 to excess Asc or Asc+GSH led to  $119 \pm 5\%$  and  $250 \pm 5\%$  increases in fluorescence, respectively.<sup>80</sup> Notably, the time required to achieve a fluorescence plateau varied significantly between **BASP-ORCA1** (approximately 40 min) and our **chex**-bottlebrush polymer (a few minutes). Collectively, these data suggest that the BASP nanostructure provides greater steric shielding and isolation of **chex** and Cy5.5 compared to the **chex**-bottlebrush polymer.

**In Vitro Cytotoxicity and in Vivo Gross Toxicity, Pharmacokinetics (PK), and Biodistribution (BD) of BASP-ORCA1 in Non-Tumor-Bearing Mice.** Next, we investigated the performance of **BASP-ORCA1** in biological assays. As discussed above, one potential advantage of ORCAs is their low toxicity. To assess the toxicity of **BASP-ORCA1**, we first conducted *in vitro* human umbilical vein endothelial cell (HUVEC) and HeLa cell viability assays. In these assays, the cells were incubated with varied concentrations of **BASP-ORCA1** for 72 h. Cell viability was determined by the CellTiter-Glo assay (Supplemental Figure S5). The half-maximal inhibitory concentrations of **BASP-ORCA1**, i.e., the concentrations that led to 50% cell death, were 1.5 mg/mL (280  $\mu\text{M}$  **chex**) and 4.5 mg/mL (830  $\mu\text{M}$  **chex**) in HUVEC and HeLa cells, respectively. These results confirm that **BASP-ORCA1** induces negligible *in vitro* cytotoxicity at practical concentrations.<sup>85,86</sup> Next, the *in vivo* gross toxicity of **BASP-ORCA1** was assessed. Healthy BALB/c mice were administered increasing doses (from 5 to 30 mg or 0.2 to 1.5 g/kg, respectively) of **BASP-ORCA1** via tail vein injection. The animal body masses and behaviors were monitored over the course of 30 days. Loss of  $\geq 10\%$  body mass is generally considered to be a sign of unacceptable toxicity.<sup>103,104</sup> As shown in Figure S6, even the highest dose of **BASP-ORCA1** (administered to  $n = 4$  animals) induced no significant decrease in body mass, which suggests that these particles are well-tolerated up to their solubility-limiting dose.

The pharmacokinetics (PK) and biodistribution (BD) of **BASP-ORCA1** were monitored in healthy, nontumor bearing BALB/c mice ( $n = 3$ ) using NIRF imaging (IVIS, Cy5.5  $\lambda_{\text{ex}}/\lambda_{\text{em}} = 640/700 \text{ nm}$ ). For PK analysis, blood samples were collected via cardiac puncture at various time points from 1 to 48 h. Percent injected dose was plotted as a function of time (Figure S7a). As is common for spherical PEGylated nanostructures, **BASP-ORCA1** exhibited a two-phase clearance behavior, with an early distribution phase of  $\sim 6$  h, followed by a steady elimination phase.<sup>67,86</sup> Fitting the data presented in Figure S7a with a standard two-compartment model yielded a blood compartment half-life for **BASP-ORCA1** of 10 h.<sup>105</sup> This long half-life is attributed to the nanoscale size of **BASP-ORCA1**, which limits renal clearance, and its PEGylated corona.<sup>66,69</sup> Consistent with these results and a plethora of studies on PEGylated nanoparticles,<sup>65–69</sup> BD analysis revealed that a majority of **BASP-ORCA1** accumulated in the liver, with increasing accumulation over 72 h (Figure S7b). Less accumulation in the kidney and negligible accumulation in other tissues was observed. Fluorescence in extracted lung tissue is attributed to a high concentration of **BASP-ORCA1** in

the blood. Notably, fluorescence images of fecal samples (Figure S7c) suggest that **BASP-ORCA1** is ultimately cleared from the body via excretion.

**BASP-ORCA1 BD in Tumor-Bearing Mice.** Given the long circulation of **BASP-ORCA1**, we hypothesized that this particle would passively accumulate in subcutaneous tumors following systemic injection. To test this hypothesis, we first established a tumor model via subcutaneous injection of a mixture of  $2.0 \times 10^6$  lung carcinoma cells (A549, ATCC), Matrigel, and PBS buffer into a hind flank of NCR-NU mice ( $n = 4$ ). When the average tumor volume was  $\sim 1$  cm, **BASP-ORCA1** was administered at a dose of 0.23 mmol **chex**/kg (1.2 g **BASP-ORCA1**/kg) via tail vein injection. NIRF images collected 20 h after administration indicated substantial tumor accumulation of **BASP-ORCA1**, which is consistent with other reports for PEGylated nanoparticles of similar size including our related drug-conjugated BASPs (Figure 4a).<sup>65,66,69,86</sup> *Ex vivo* BD data were consistent with our studies on nontumor bearing BALB/c mice (i.e., liver accumulation and persistence in blood) with the addition of significant tumor accumulation (Figure 4b and Figure S8).

**MRI and NIRF Imaging with **BASP-ORCA1** in Tumor-Bearing Mice.** The low toxicity, long circulation half-life, and tumor accumulation of **BASP-ORCA1**, along with its exceptional stability and relaxivity, suggested that this particle could be suitable for MRI of tumors following systemic injection and accumulation; a feat that, to our knowledge, has not yet been achieved with ORCAs. Two groups of A459 tumor-bearing NCR-NU mice were administered different doses of **BASP-ORCA1** via tail-vein injection: the “low dose” group ( $n = 3$ ) received 0.16 mmol **chex**/kg (0.8 g **BASP-ORCA1**/kg), while the “high dose” group ( $n = 4$ ) received 0.23 mmol **chex**/kg (1.2 g **BASP-ORCA1**/kg). The mice were anaesthetized and MR images were collected at various time points: 12, 16, and 20 h postinjection for the low dose group and 20 h postinjection for the high dose group. The images from each time point were compared to images collected before **BASP-ORCA1** injection. Figure 5a shows  $T_2$ -weighted false-colored images for a selected mouse from the low dose group imaged before **BASP-ORCA1** injection (top row of images) and 20 h (bottom row of images) after **BASP-ORCA1** injection. From left-to-right the images correspond to progressive slices of the same animal in the  $z$ -axis with the tumor indicated with a yellow arrow in each image. Figure 5b shows an analogous set of images for a selected mouse from the high dose group. Contrast differences between the preinjection and postinjection images can be observed at both dose levels, with greater contrast observed in the high dose animal (Figure 5b). Whole animal images similarly revealed a clear difference in tumor contrast (Figure 5c, yellow arrows).

The percent negative contrast enhancement (i.e., the amount of signal reduction) before and after **BASP-ORCA1** administration was quantified by image analysis (Figure 5d). Signal reductions ranging from  $14 \pm 2\%$  to  $16 \pm 2\%$  ( $P \leq 0.05$ ) were observed for the 12 to 20 h time points in the low dose group (Figure 5d, red bars). In the high dose group, a  $24 \pm 2\%$  ( $P \leq 0.001$ ) signal reduction was observed 20 h after **BASP-ORCA1** administration (Figure 5d, blue bar). The **BASP-ORCA1** dose–response effect suggests that the observed contrast differences between pre- and postinjection are due to accumulation of **BASP-ORCA1** in the tumors. Keeping in mind that MRI phantoms revealed no observable contrast enhancement for PEG-BASPs that lack **chex** (Figure 2c), these

MRI data imply that 20 h following injection there is a sufficient concentration of **chex** radicals present on the **BASP-ORCA1** in the tumor to impart contrast. To confirm the presence of **chex** radicals in the tumors, the same mice that were imaged by MRI were sacrificed 21 h after **BASP-ORCA1** administration and their tissue homogenates and blood were analyzed by EPR spectroscopy (Figure 6a). From these spectra, the radical concentration per gram of protein in each tissue sample, the latter obtained via a bicinchoninic acid assay (BCA), was evaluated and normalized by the radical concentration per gram of protein in muscle tissue (Figure 6b). In agreement with our MRI data, the concentration of free radicals in the tumor was quite high after **BASP-ORCA1** injection; the measured value of  $0.25 \pm 0.04 \mu\text{mol chex/g}$  of protein corresponds to 4.5% of the injected dose of **chex** radicals. Moreover, consistent with our *in vivo* NIRF imaging results (*vide supra*), relatively high radical concentrations were observed in the liver and kidney, which suggests that the clearance of **BASP-ORCA1** proceeded mostly through these organs. Notably, the murine liver contains a high concentration of Asc (millimolar range); our observation of radicals in the liver is further evidence of the extremely stable nature of the **chex** units in **BASP-ORCA1** (*Note*: in our previous **chex**-bottlebrush polymers, there was very little **chex** radical in the liver following 30 min and none observed after 24 h). A high **chex** concentration was also observed in the heart, which is in accord with a long blood compartment half-life and is consistent with our PK data obtained by NIRF imaging. Finally, NIRF imaging of these homogenates provided fluorescence radiant efficiencies that were in good agreement with our spin concentrations (Figure 6b), which suggests that the **chex** radicals and Cy5.5 dyes are still colocalized within the **BASP-ORCA1** construct after biodistribution. Unlike our previous **chex**-bottlebrush polymers, which displayed dramatic increases in fluorescence as **chex** was reduced, the signal uniformity offered by **BASP-ORCA1** provides for straightforward multimodal confirmation of BD.

To the best of our knowledge, **BASP-ORCA1** is the first nitroxide MRI contrast agent capable of providing significant contrast 20 h after injection, which is a testament to its unique structural features that combine optimal size for tumor accumulation with a high nitroxide density and stability. To set these results in context, we compared our data to recent literature examples of MRI-contrast agents that rely on metals to achieve tumor imaging following systemic administration. For example, Kataoka and co-workers recently reported on a new class of Gd-based nanoparticles ( $T_1$  contrast agents) for MRI of tumors. In their study, a  $\sim 40\%$  contrast enhancement (at 0.05 mmol Gd/kg iv dose) was observed 4 h following injection into mice bearing subcutaneous C26 tumors. Notably, the commercially available small molecule contrast agent Gd-DTPA exhibited negligible contrast enhancement (at 0.23 mmol Gd/kg iv dose) after 4 h.<sup>16</sup> This example highlights the importance of a nanoparticle system for extended circulation and tumor imaging. The same group reported Fe-based nanoparticles ( $T_2$  contrast agents) for tumor imaging in a similar murine model (subcutaneous C26 tumors). Here, an approximately 25% contrast difference was observed 24 h following intravenous administration of 0.45 mg Fe/kg. Notably, less than 10% contrast enhancement was observed using commercially available Resovist (at 0.45 mg Fe/kg intravenous dose).<sup>15</sup> It should be noted that the instrument parameters used to obtain  $T_2$ -weighted images in this work



were similar to those used above in our studies; thus, our results for **BASP-ORCA1** are on par with recently reported nanoparticle MRI contrast agents that rely on metals to achieve contrast.

## CONCLUSION

We have developed a nitroxide-based macromolecular MRI contrast agent —**BASP-ORCA1**— that enables simultaneous MRI and NIRF imaging *in vivo* over time scales suitable for tumor imaging following systemic injection. **BASP-ORCA1** addresses the two major challenges that have historically limited nitroxide-based organic radical contrast agents for MRI: low relaxivity and poor stability. These functions were made possible by the brush-arm star polymer (BASP) nanostructure, which places a dense layer of **chex** nitroxides at the interface between a rigid poly(acetal) core and a hydrophilic PEG shell. Altogether, **BASP-ORCA1** displayed unprecedented per-nitroxide and per-molecule transverse relaxivities for organic radical contrast agents, exceptional stability, high water solubility, low *in vitro* and *in vivo* toxicity, and a long blood compartment half-life. These features combined to facilitate the imaging of subcutaneous tumors in mice 20 h after tail-vein injection, providing contrast enhancements on par with commercial and literature examples of metal-based contrast agents. This work suggests that organic radicals can be viable alternatives to metal-based MRI contrast agents, and sets the stage for the development of theranostic systems that combine organic radical contrast agents with therapeutic payloads to achieve simultaneous tumor imaging and drug delivery without concerns over long-term tissue accumulation of metals.

## ASSOCIATED CONTENT

### Supporting Information

The Supporting Information is available free of charge on the ACS Publications website at DOI: [10.1021/acscentsci.7b00253](https://doi.org/10.1021/acscentsci.7b00253).

Synthesis and characterization data for BASPs, as well as supplementary figures, methods and materials, experimental procedures, *in vitro*, *in vivo*, and *ex vivo* supplementary data (PDF)

## AUTHOR INFORMATION

### Corresponding Author

\*E-mail: [jaj2109@mit.edu](mailto:jaj2109@mit.edu).

### ORCID

Qixian Chen: 0000-0002-3091-671X

M. Francesca Ottaviani: 0000-0002-4681-4718

Andrzej Rajca: 0000-0002-8856-1536

Jeremiah A. Johnson: 0000-0001-9157-6491

### Notes

The authors declare no competing financial interest.

## ACKNOWLEDGMENTS

We thank the NIH-NIBIB (1R21EB018529-01A1 for J.A.J. and A.R.; R01 EB-019950-01A1 for A.R.) and the National Science Foundation (Graduate Research Fellowship for H.V.-T.N.) for support of this research. A.J. thanks the NIH (U01-NS090451). P.H. was supported by a Wellcome Trust-MIT Postdoctoral Fellowship. This work was supported in part by the Koch Institute Support (core) Grant P30-CA14051 from the National Cancer Institute. We thank the Koch Institute Swanson Biotechnology Center for technical support, specifi-

cally Dr. S. Malstrom and Ms. W. Huang. We thank Dr. A. Detappe and Dr. P. Ghoroghchian for very fruitful discussions and consultations.

## DEDICATION

¶We dedicate this work to our co-author, Michael D. Boska, who passed away on May 13, 2017 in a one-man hang glider accident. Hang gliding was Mike's hobby and his dream come true for nearly 40 years. He spent his last moments doing what he loved. This loss is tremendous on multiple levels. Mike was an incredible asset to our research, the community, and the University of Nebraska Medical Center. His contributions will positively impact the medical field for years to come.

## REFERENCES

- (1) Cheon, J.; Lee, J.-H. Synergistically Intergrated Nanoparticles as Multimodal Probes for Nanobiotechnology. *Acc. Chem. Res.* **2008**, *41*, 1630–1640.
- (2) Na, H. B.; Song, I. C.; Hyeon, T. Inorganic Nanoparticles for MRI Contrast Agents. *Adv. Mater.* **2009**, *21*, 2133–2148.
- (3) Lee, D.-E.; Koo, H.; Sun, I.-C.; Ryu, J. H.; Kim, K.; Kwon, I.-C. Multifunctional Nanoparticles for Multimodal Imaging and Theragnosis. *Chem. Soc. Rev.* **2012**, *41*, 2656–2672.
- (4) Villaraza, A. J. L.; Bumb, A.; Brechbiel, M. W. Macromolecules, Dendrimers, and Nanomaterials in Magnetic Resonance Imaging: The Interplay between Size, Function, and Pharmacokinetics. *Chem. Rev.* **2010**, *110*, 2921–2959.
- (5) Davies, G.-L.; Kramberger, I.; Davis, J. J. Environmentally Responsive MRI Contrast Agents. *Chem. Commun.* **2013**, *49*, 9704–9721.
- (6) Mastarone, D. J.; Harrison, V. S. R.; Eckermann, A. L.; Parigi, G.; Luchinat, C.; Meade, T. J. A Modular System for the Synthesis of Multiplexed Magnetic Resonance Probes. *J. Am. Chem. Soc.* **2011**, *133*, 5329–5337.
- (7) Caravan, P.; Ellison, J. J.; McMurry, T. J.; Lauffer, R. B. Gadolinium (III) Chelates as MRI Contrast Agents: Structure, Dynamics, and Applications. *Chem. Rev.* **1999**, *99*, 2293–2352.
- (8) Tu, C.; Nagao, R.; Louie, A. Y. Multimodal Magnetic-resonance/Optical-imaging Contrast Agent Sensitive to NADH. *Angew. Chem., Int. Ed.* **2009**, *48*, 6547–6551.
- (9) Harrison, V. S. R.; Carney, C. E.; MacRenaris, K. W.; Meade, T. J. A Multimeric MR-optical Contrast Agent for Multimodal Imaging. *Chem. Commun.* **2014**, *50*, 11469–11471.
- (10) Harrison, V. S. R.; Carney, C. E.; MacRenaris, K. W.; Waters, E. A.; Meade, T. J. Multimeric Near IR-MR Contrast Agent for Multimodal *in vivo* Imaging. *J. Am. Chem. Soc.* **2015**, *137*, 9108–9116.
- (11) MacRenaris, K. W.; Ma, Z.; Krueger, R. L.; Carney, C. E.; Meade, T. J. Cell-permeable Esterase-activated Ca(II)-Sensitive MRI Contrast Agent. *Bioconjugate Chem.* **2016**, *27*, 465–473.
- (12) You, Y.; Tomat, E.; Hwang, K.; Atanasijevic, T.; Nam, W.; Jasanoff, A. P.; Lippard, S. Manganese Displacement from Zinpyr-1 Allows Zinc Detection by Fluorescence Microscopy and Magnetic Resonance Imaging. *Chem. Commun.* **2010**, *46*, 4139–4141.
- (13) Zhang, X.; Jing, X.; Liu, T.; Han, G.; Li, H.; Duan, C. Dual-functional Gadolinium-based Copper(II) Probe for Selective Magnetic Resonance Imaging and Fluorescence Sensing. *Inorg. Chem.* **2012**, *51*, 2325–2331.
- (14) Mi, P.; Kokuryo, D.; Cabral, H.; Wu, H.; Terada, Y.; Saga, T.; Aoki, I.; Nishiyama, N.; Kataoka, K. A pH-activatable Nanoparticle with Signal-amplification Capabilities for non-invasive Imaging of Tumor Malignancy. *Nat. Nanotechnol.* **2016**, *11*, 724–730.
- (15) Kokuryo, D.; Anraku, Y.; Kishimura, A.; Tanaka, S.; Kano, M. R.; Kershaw, J.; Nishiyama, N.; Saga, T.; Aoki, I.; Kataoka, K. SPIO-PICsome: Development of a Highly Sensitive and Stealth-capable MRI Nano-agent for Tumor Detection using SPIO-loaded Unilamellar Polyion Complex Vesicles (PICsomes). *J. Controlled Release* **2013**, *169*, 220–227.

- (16) Mi, P.; Kokuryo, D.; Cabral, H.; Kumagai, M.; Nomoto, T.; Aoki, I.; Terada, Y.; Kishimura, A.; Nishiyama, N.; Kataoka, K. Hydrothermally Synthesized PEGylated Calcium Phosphate Nanoparticles Incorporating Gd-DTPA for Contrast Enhanced MRI Diagnosis of Solid Tumors. *J. Controlled Release* **2014**, *174*, 63–71.
- (17) Chou, S.-W.; Shau, Y.-H.; Wu, P.-C.; Yang, Y.-S.; Shieh, D.-B.; Chen, C.-C. *in vitro* and *in vivo* Studies of FePt Nanoparticles for Dual Modal CT/MRI Molecular Imaging. *J. Am. Chem. Soc.* **2010**, *132*, 13270–13278.
- (18) Holbrook, R. J.; Rammohan, N.; Rotz, M. W.; MacRenaris, K. W.; Preslar, A. T.; Meade, T. J. Gd(III)-dithiolane Gold Nanoparticles for T1-Weighted Magnetic Resonance Imaging of the Pancreas. *Nano Lett.* **2016**, *16*, 3202–3209.
- (19) Nicholls, F. J.; Rotz, M. W.; Ghuman, H.; MacRenaris, K. W.; Meade, T. J.; MODO, M. DNA-gadolinium-gold Nanoparticles for *in vivo* T1MR Imaging of Transplanted Human Neural Stem Cells. *Biomaterials* **2016**, *77*, 291–306.
- (20) Choi, J.-S.; Lee, J.-H.; Shin, T.-H.; Song, H.-T.; Kim, E. Y.; Cheon, J. Self-confirming “AND” Logic Nanoparticles for Fault-free MRI. *J. Am. Chem. Soc.* **2010**, *132*, 11015–11017.
- (21) Medarova, Z.; Pham, W.; Farrar, C.; Petkova, V.; Moore, A. *in vivo* Imaging of siRNA Delivery and Silencing in Tumors. *Nat. Med.* **2007**, *13*, 372–377.
- (22) Shellock, F. G.; Kanal, E. Safety of Magnetic Resonance Imaging Contrast Agents. *J. Magn. Reson. Imaging*. **1999**, *10*, 477–484.
- (23) Swaminathan, S.; Horn, T. D.; Pellowski, D.; Abul-Ezz, S.; Bornhorst, J. A.; et al. Nephrogenic Systemic Fibrosis, Gadolinium, and Iron Mobilization. *N. Engl. J. Med.* **2007**, *357*, 720–722.
- (24) Shin, T.-H.; Choi, Y.; Kim, S.; Cheon, J. Recent Advances in Magnetic Nanoparticle-based Multi-modal Imaging. *Chem. Soc. Rev.* **2015**, *44*, 4501–4516.
- (25) Verwilt, P.; Park, S.; Yoon, B.; Kim, J. S. Recent Advances in Gd-chelate Based Bimodal Optical/MRI Contrast Agents. *Chem. Soc. Rev.* **2015**, *44*, 1791–1806.
- (26) Mendichovszky, I. A.; Marks, S. D.; Simcock, C. M.; Olsen, O. E. Gadolinium and Nephrogenic Systemic Fibrosis: Time to Tighten Practice. *Pediatr. Radiol.* **2008**, *38*, 489–496.
- (27) Hatje, V.; Bruland, K. W.; Flegal, A. R. Increases in Anthropogenic Gadolinium Anomalies and Rare Earth Element Concentration in San Francisco Bay over a 20 Year Record. *Environ. Sci. Technol.* **2016**, *50*, 4159–4168.
- (28) Nardone, B.; Saddleton, E.; Laumann, A. E.; Edwards, B. J.; Raisch, D. W.; McKoy, J. M.; Belknap, S. M.; Bull, C.; Haryani, A.; Cowper, S. E.; Abu-Alfa, A. K.; Miller, F. H.; Godinez-Puig, V.; Dharnidharka, V. R.; West, D. P. Pediatric Nephrogenic Systemic Fibrosis is Rarely Reported: a RADAR Report. *Pediatr. Radiol.* **2014**, *44*, 173–180.
- (29) We thank one of the reviewers for pointing out to us safety issues associated with  $T_2$  contrast agents based on iron-nanoparticles.
- (30) Wang, Y.-X. J. Superparamagnetic Iron Oxide Based MRI Contrast Agents: Current Status of Clinical Application. *Quant. Imaging. Med. Surg.* **2011**, *1*, 35–40.
- (31) Wang, Y.-X. J. Current Status of Superparamagnetic Iron Oxide Contrast Agents for Liver Magnetic Resonance Imaging. *World J. Gastroenterol.* **2015**, *21*, 13400–13402.
- (32) Feng, J.; Liu, H.; Bhakoo, K. K.; Lu, L.; Chen, Z. A Metabonomic Analysis of Organ Specific Response to USPIO Administration. *Biomaterials* **2011**, *32*, 6558–6569.
- (33) Vasanawala, S. S.; Nguyen, K.-L.; Hope, M. D.; Bridges, M. D.; Hope, T. A.; Reeder, S. B.; Bashir, M. R. Safety and Technique of Ferumoxytol Administration for MRI. *Magn. Reson. Med.* **2016**, *75*, 2107–2111.
- (34) Thakor, A. S.; Jokerst, J. V.; Ghanouni, P.; Campbell, J. L.; Mittra, E.; Gambhir, S. S. Clinically Approved Nanoparticle Imaging Agents. *J. Nucl. Med.* **2016**, *57*, 1833–1837.
- (35) *Feraheme (Ferumoxytol): Drug Safety Communication – Warnings Strengthened and Prescribing Instruction Changed*; U. S. Food & Drug Administration (FDA), 2015, <https://www.fda.gov/safety/medwatch/safetyinformation/safetyalertsforhumanmedicalproducts/ucm440479.htm>.
- (36) Lim, Y. T.; Noh, Y.-W.; Cho, J.-H.; Han, J. H.; Choi, B. S.; Kwon, J.; Hong, K. S.; Gokarna, A.; Cho, Y.-H.; Chung, B. H. Multiplexed Imaging of Therapeutic Cells with Multispectrally Encoded Magnetofluorescent Nanocomposite Emulsions. *J. Am. Chem. Soc.* **2009**, *131*, 17145–17154.
- (37) Rolfe, B. E.; Blakey, I.; Squires, O.; Peng, H.; Boase, N. R. B.; Alexander, C.; Parsons, P. G.; Boyle, G. M.; Whittaker, A. K.; Thurecht, K. J. Multimodal Polymer Nanoparticles with Combined  $^{19}\text{F}$  Magnetic Resonance and Optical Detection for Tunable, Targeted, Multimodal Imaging *in vivo*. *J. Am. Chem. Soc.* **2014**, *136*, 2413–2419.
- (38) Patrick, M. J.; Janjic, J. M.; Teng, H.; O’Hear, M. R.; Brown, C. W.; Stokum, J. A.; Schmidt, B. F.; Ahrens, E. T.; Waggoner, A. S. Intracellular pH Measurements Using Perfluorocarbon Nanoemulsions. *J. Am. Chem. Soc.* **2013**, *135*, 18445–18457.
- (39) Bar-Shir, A.; Yadav, N. N.; Gilad, A. A.; van Zijl, P. C. M.; McMahon, M. T.; Bulte, J. W. M. Single  $^{19}\text{F}$  Probe for Simultaneous Detection of Multiple Metal Ions Using *in vivo*  $\mu\text{CEST}$  MRI. *J. Am. Chem. Soc.* **2015**, *137*, 78–81.
- (40) Lock, L. L.; Li, Y.; Mao, X.; Chen, H.; Staedtke, V.; Bai, R.; Ma, W.; Lin, R.; Li, Y.; Liu, G.; Cui, H. One-component Supramolecular Filament Hydrogels as Theranostic Label-free Magnetic Resonance Imaging Agents. *ACS Nano* **2017**, *11*, 797–805.
- (41) Ferrauto, G.; Di Gregorio, E.; Baroni, S.; Aime, S. Frequency-encoded MRI-CEST Agents Based on Paramagnetic Liposomes/RBC Aggregates. *Nano Lett.* **2014**, *14*, 6857–6862.
- (42) Ratnakar, S. J.; Soesbe, T. C.; Lumata, L. L.; Do, Q. N.; Viswanathan, S.; Lin, C.-Y.; Sherry, A. D.; Kovacs, Z. Modulation of CEST Images *in vivo* by  $T_1$  Relaxation: a New Approach in the Design of Responsive PARACEST Agents. *J. Am. Chem. Soc.* **2013**, *135*, 14904–14907.
- (43) Ferrauto, G.; Delli Castelli, D.; Di Gregorio, E.; Langereis, S.; Burdinski, D.; Grull, H.; Terreno, E.; Aime, S. Lanthanide-loaded Erythrocytes as Highly Sensitive Chemical Exchange Saturation Transfer MRI Contrast Agents. *J. Am. Chem. Soc.* **2014**, *136*, 638–641.
- (44) Terreno, E.; Castelli, D. D.; Viale, A.; Aime, S. Challenges for Molecular Magnetic Resonance Imaging. *Chem. Rev.* **2010**, *110*, 3019–3042.
- (45) Glunde, K.; Artemov, D.; Penet, M.-F.; Jacobs, M. A.; Bhujwala, Z. M. Magnetic Resonance Spectroscopy in Metabolic and Molecular Imaging and Diagnostic of Cancer. *Chem. Rev.* **2010**, *110*, 3043–3059.
- (46) Smith, B. R.; Gambhir, S. S. Nanomaterials for *In Vivo* Imaging. *Chem. Rev.* **2017**, *117*, 901–986.
- (47) Harvey, P.; Kuprov, I.; Parker, D. Lanthanide Complexes as Paramagnetic Probes for  $^{19}\text{F}$  Magnetic Resonance. *Eur. J. Inorg. Chem.* **2012**, *2012*, 2015–2022.
- (48) Boase, N. R. B.; Blakey, I.; Thurecht, K. J. Molecular Imaging with Polymers. *Polym. Chem.* **2012**, *3*, 1384–1389.
- (49) Tirotta, I.; Dichiarante, V.; Pigliacelli, C.; Cavallo, G.; Terraneo, G.; Bombelli, F. B.; Metrangolo, P.; Resnati, G.  $^{19}\text{F}$  Magnetic Resonance Imaging (MRI): From Design of Materials to Clinical Applications. *Chem. Rev.* **2015**, *115*, 1106–1129.
- (50) Aime, S.; Castelli, D. D.; Crich, S. G.; Gianolio, E.; Terreno, E. Pushing the Sensitivity Envelope of Lanthanide-based Magnetic Resonance Imaging (MRI) Contrast Agents for Molecular Imaging Applications. *Acc. Chem. Res.* **2009**, *42*, 822–831.
- (51) Liu, G.; Song, X.; Chan, K. W. Y.; McMahon, M. T. Nuts and Bolts of Chemical Exchange Saturation Transfer MRI. *NMR Biomed.* **2013**, *26*, 810–828.
- (52) Rajca, A.; Wang, Y.; Boska, M.; Paletta, J. T.; Olankitwanit, A.; Swanson, M. A.; Mitchell, D. G.; Eaton, S. S.; Eaton, G. R.; Rajca, S. Organic Radical Contrast Agents for Magnetic Resonance Imaging. *J. Am. Chem. Soc.* **2012**, *134*, 15724–15727.
- (53) Rajca, A.; Wang, Y.; Boska, M.; Paletta, J. T.; Olankitwanit, A.; Swanson, M. A.; Mitchell, D. G.; Eaton, S. S.; Eaton, G. R.; Rajca, S. Correction to Organic Radical Contrast Agents for Magnetic Resonance Imaging. *J. Am. Chem. Soc.* **2014**, *136*, 3318–3318.

- (54) Hyodo, F.; Soule, B. P.; Matsumoto, K.-I.; Matusmoto, S.; Cook, J. A.; Hyodo, E.; Sowers, A. L.; Krishna, M. C.; Mitchell, J. B. Assessment of Tissue Redox Status Using Metabolic Responsive Contrast Agents and Magnetic Resonance Imaging. *J. Pharm. Pharmacol.* **2008**, *60*, 1049–1060.
- (55) Hyodo, F.; Chuang, K.-H.; Goloshevsky, A. G.; Sulima, A.; Griffiths, G. L.; Mitchell, J. B.; Koretsky, A. P.; Krishna, M. C. Brain Redox Imaging Using Blood-brain Barrier-permeable Nitroxide MRI Contrast Agent. *J. Cereb. Blood Flow Metab.* **2008**, *28*, 1165–1174.
- (56) Brasch, R. C. Work in Progress: Methods of Contrast Enhancement for NMR Imaging and Potential Applications. A Subject Review. *Radiology* **1983**, *147*, 781–788.
- (57) Brasch, R. C.; London, D. A.; Wesbey, G. E.; Tozer, T. N.; Nitecki, D. E.; Williams, R. D.; Doemeny, J.; Tuck, L. D.; Lallemand, D. P. Work in Progress: Nuclear Magnetic Resonance Study of a Paramagnetic Nitroxide Contrast Agent for Enhancement of Renal Structures in Experimental Animals. *Radiology* **1983**, *147*, 773–779.
- (58) Matsumoto, K.-I.; Hyodo, F.; Matsumoto, A.; Koretsky, A. P.; Sowers, A. L.; Mitchell, J. B.; Krishna, M. C. High-resolution Mapping of Tumor Redox Status by Magnetic Resonance Imaging Using Nitroxides as Redox-sensitive Contrast Agents. *Clin. Cancer Res.* **2006**, *12*, 2455–2462.
- (59) Hyodo, F.; Matsumoto, K.-I.; Matsumoto, A.; Mitchell, J. B.; Krishna, M. C. Probing the Intracellular Redox Status of Tumors with Magnetic Resonance Imaging and Redox-sensitive Contrast Agents. *Cancer Res.* **2006**, *66*, 9921–9928.
- (60) Zhelev, Z.; Bakalova, R.; Aoki, I.; Lazarova, D.; Saga, T. Imaging of Superoxide Generation in the Dopaminergic Area of the Brain in Parkinson's Disease, Using Mito-TEMPO. *ACS Chem. Neurosci.* **2013**, *4*, 1439–1445.
- (61) Davis, R. M.; Sowers, A. L.; Degraff, W.; Bernardo, M.; Thetford, A.; Krishna, M. C.; Mitchell, J. B. A Novel Nitroxide is an Effective Brain Redox Imaging Contrast Agent and *in vivo* Radioprotector. *Free Radical Biol. Med.* **2011**, *51*, 780–790.
- (62) Zhelev, Z.; Bakalova, R.; Aoki, I.; Matsumoto, K.-I.; Gadjeva, V.; Anzai, K.; Kanno, I. Nitroxide Radicals for Labelling of Conventional Therapeutics and Noninvasive Magnetic Resonance Imaging of Their Permeability for Blood-brain Barrier: Relationship between Structure, Blood Clearance, and MRI Signal Dynamic in the Brain. *Mol. Pharmaceutics* **2009**, *6*, 504–512.
- (63) Doane, T. L.; Burda, C. The Unique Role of Nanoparticles in Nanomedicine: Imaging, Drug Delivery and Therapy. *Chem. Soc. Rev.* **2012**, *41*, 2885–2911.
- (64) Jokerst, J. V.; Gambhir, S. S. Molecular Imaging with Theranostic Nanoparticles. *Acc. Chem. Res.* **2011**, *44*, 1050–1060.
- (65) Joralemon, M. J.; McRae, S.; Emrick, T. PEGylated Polymers for Medicine: from Conjugation to Self-assembled Systems. *Chem. Commun.* **2010**, *46*, 1377–1393.
- (66) Torchilin, V. Tumor Delivery of Macromolecular Drugs Based on the EPR Effect. *Adv. Drug Delivery Rev.* **2011**, *63*, 131–135.
- (67) Anraku, Y.; Kishimura, A.; Kobayashi, A.; Oba, M.; Kataoka, K. Size-controlled Long-circulating PICsome as a Ruler to Measure Critical Cut-off Disposition Size into Normal and Tumor Tissues. *Chem. Commun.* **2011**, *47*, 6054–6056.
- (68) Cabral, H.; Matsumoto, Y.; Mizuno, K.; Chen, Q.; Murakami, M.; Kimura, M.; Terada, Y.; Kano, M. R.; Miyazono, K.; Uesaka, M.; Nishiyama, N.; Kataoka, K. Accumulation of Sub-100 nm Polymeric Micelles in Poorly Permeable Tumours Depends on Size. *Nat. Nanotechnol.* **2011**, *6*, 815–823.
- (69) Jokerst, J. V.; Lobovkina, T.; Zare, R. N.; Gambhir, S. S. Nanoparticle PEGylation for Imaging and Therapy. *Nanomedicine* **2011**, *6*, 715–728.
- (70) Elliott, K. A. Metabolism of brain tissue slices and suspensions from various mammals. *J. Neurophysiol.* **1948**, *11*, 473–484.
- (71) Tolmasoff, J. M.; Ono, T.; Cutler, R. G. Superoxide dismutase: correlation with lifespan and specific metabolic rate in primate species. *Proc. Natl. Acad. Sci. U. S. A.* **1980**, *77*, 2777–2781.
- (72) Zhelev, Z.; Bakalova, R.; Aoki, I.; Matsumoto, K.-I.; Gadjeva, V.; Anzai, K.; Kanno, I. Nitroxyl Radicals as Low Toxic Spin-labels for Non-invasive Magnetic Resonance Imaging of Blood-brain Barrier Permeability for Conventional Therapeutics. *Chem. Commun.* **2009**, 53–55.
- (73) Samuni, Y.; Gamson, J.; Samuni, A.; Yamada, K.; Russo, A.; Krishna, M. C.; Mitchell, J. B. Factors Influencing Nitroxide Reduction and Cytotoxicity *in Vitro*. *Antioxid. Redox Signaling* **2004**, *6*, 587–595.
- (74) Merbach, A. S.; Helm, L.; Toth, E. *The Chemistry of Contrast Agent in Medical Magnetic Resonance Imaging*, 2nd ed.; John Wiley & Sons: Chichester, 2013.
- (75) Caravan, P. Protein-targeted Gadolinium-based Magnetic Resonance Imaging (MRI) Contrast Agents: Design and Mechanism of Action. *Acc. Chem. Res.* **2009**, *42*, 851–862.
- (76) Winalski, C. S.; Shortkroff, S.; Mulkern, R. V.; Schneider, E.; Rosen, G. M. Magnetic Resonance Relaxivity of Dendrimer-linked Nitroxides. *Magn. Reson. Med.* **2002**, *48*, 965–972.
- (77) Winalski, C. S.; Shortkroff, S.; Schneider, E.; Yoshioka, H.; Mulkern, R. V.; Rosen, G. M. Targeted Dendrimer-based Contrast Agents for Articular Cartilage Assessment by MR Imaging. *Osteoarthr. Cartil.* **2008**, *16*, 815–822.
- (78) Francese, G.; Dunand, F. A.; Loosli, C.; Merbach, A. E.; Decurtins, S. Functionalization of PAMAM Dendrimers with Nitronyl Nitroxide Radicals as Models for the Outer-sphere Relaxation in Dendritic Potential MRI Contrast Agents. *Magn. Reson. Chem.* **2003**, *41*, 81–83.
- (79) Paletta, J. T.; Pink, M.; Foley, B.; Rajca, S.; Rajca, A. Synthesis and Reduction Kinetics of Sterically Shielded Pyrrolidine Nitroxides. *Org. Lett.* **2012**, *14*, 5322–5325.
- (80) Sowers, M. A.; McCombs, J. R.; Wang, Y.; Paletta, J. T.; Morton, S. W.; Dreaden, E. C.; Boska, M. D.; Ottaviani, M. F.; Hammond, P. T.; Rajca, A.; Johnson, J. A. Redox Responsive Branched Bottebrush Polymers for *In Vivo* MRI and Fluorescence Imaging. *Nat. Commun.* **2014**, *5*, 5460.
- (81) Xia, Y.; Li, Y.; Burts, A. O.; Ottaviani, M. F.; Tirrell, D. A.; Johnson, J. A.; Turro, N. J.; Grubbs, R. H. EPR Study of Spin Labeled Brush Polymers in Organic Solvents. *J. Am. Chem. Soc.* **2011**, *133*, 19953–19959.
- (82) Burts, A. O.; Li, Y.; Zhukhovitskiy, A. V.; Patel, P. R.; Grubbs, R. H.; Ottaviani, M. F.; Turro, N. J.; Johnson, J. A. Using EPR to Compare PEG-branch-nitroxide “Bivalent-brush Polymers” and Traditional PEG Bottle-brush Polymers: Branching Makes a Difference. *Macromolecules* **2012**, *45*, 8310–8318.
- (83) Liu, J.; Burts, A. O.; Li, Y.; Zhukhovitskiy, A. V.; Ottaviani, M. F.; Turro, N. J.; Johnson, J. A. Brush-first” Method for the Parallel Synthesis of Photocleavable, Nitroxide-labeled poly(ethylene glycol) Star Polymers. *J. Am. Chem. Soc.* **2012**, *134*, 16337–16344.
- (84) Gao, A. X.; Liao, L.; Johnson, J. A. Synthesis of Acid-labile PEG and PEG-doxorubicin-conjugate Nanoparticles via Brush-first ROMP. *ACS Macro Lett.* **2014**, *3*, 854–857.
- (85) Liao, L.; Liu, J.; Dreaden, E. C.; Morton, S. W.; Shopsowitz, K. E.; Hammond, P. T.; Johnson, J. A. A Convergent Synthetic Platform for Single-nanoparticle Combination Cancer Therapy: Ratiometric Loading and Controlled Release of Cisplatin, Doxorubicin, and Camptothecin. *J. Am. Chem. Soc.* **2014**, *136*, 5896–5899.
- (86) Barnes, J. C.; Bruno, P. M.; Nguyen, H. V.-T.; Liao, L.; Liu, J.; Hemann, M. T.; Johnson, J. A. Using an RNAi Signature Assay to Guide the Design of Three-drug Conjugated Nanoparticles with Validated Mechanisms, *in vivo* Efficacy, and Low Toxicity. *J. Am. Chem. Soc.* **2016**, *138*, 12494–12501.
- (87) Liu, J.; Gao, A. X.; Johnson, J. A. Particles Without a Box: Brush-first Synthesis of Photodegradable PEG Star Polymers under Ambient Conditions. *J. Visualized Exp.* **2013**, *80*, e50874.
- (88) Burts, A. O.; Liao, L.; Lu, Y. Y.; Tirrell, D. A.; Johnson, J. A. Brush-first and Click: Efficient Synthesis of Nanoparticles that Degrade and Release Doxorubicin in Response to Light. *Photochem. Photobiol.* **2014**, *90*, 380–385.
- (89) Love, J. A.; Morgan, J. P.; Trnka, T. M.; Grubbs, R. H. A Practical and Highly Active Ruthenium-based Catalyst that Effects the Cross Metathesis of Acrylonitrile. *Angew. Chem., Int. Ed.* **2002**, *41*, 4035–4037.

(90) Budil, D. E.; Lee, S.; Saxena, S.; Freed, J. H. Nonlinear-least-square Analysis of Slow-motion EPR Spectra in One and Two Dimensions Using a Modified Levenberg-Marquardt-algorithm. *J. Magn. Reson., Ser. A* **1996**, *120*, 155–189.

(91) Na, H. B.; Lee, J. H.; An, K.; Park, Y. I.; Park, M.; Lee, I. S.; Nam, D.-H.; Kim, S. T.; Kim, S.-H.; Kim, S.-W.; et al. Development of a T1 Contrast Agent for Magnetic Resonance Imaging Using MnO Nanoparticles. *Angew. Chem., Int. Ed.* **2007**, *46*, 5397–5401.

(92) Detappe, A.; Kunjachan, S.; Sancey, L.; Motto-Ros, V.; Biancur, D.; Drane, P.; Guieze, R.; Makrigiorgos, G. M.; Tillement, O.; Langer, R.; et al. Advanced multimodal nanoparticles delay tumor progression with clinical radiation therapy. *J. Controlled Release* **2016**, *238*, 103–113.

(93) Sancey, L.; Kotb, S.; Truillet, C.; Appaix, F.; Marais, A.; Thomas, E.; van der Sanden, B.; Klein, J. P.; Laurent, B.; Cottier, M.; et al. Long-Term in Vivo Clearance of Gadolinium-Based AGuIX Nanoparticles and Their Biocompatibility after Systemic Injection. *ACS Nano* **2015**, *9*, 2477–2488.

(94) Wei, H.; Bruns, O. T.; Kaul, M. G.; Hansen, E. C.; Barch, M.; Wisniowska, A.; Chen, O.; Chen, Y.; Li, N.; Okada, S.; Cordero, J. M.; Heine, M.; Farrar, C. T.; Montana, D. M.; Adam, G.; Ittrich, H.; Jasanoff, A.; Nielsen, P.; Bawendi, M. G. Exceedingly Small Iron Oxide Nanoparticles as Positive MRI Contrast Agents. *Proc. Natl. Acad. Sci. U. S. A.* **2017**, *114*, 2325–2330.

(95) Li, Y.; Lei, X.; Jockusch, S.; Chen, J. Y.-C.; Frunzi, M.; Johnson, J. A.; Lawler, R. G.; Murata, Y.; Murata, M.; Komatsu, K.; Turro, N. J. A Magnetic Switch for Spin-catalyzed Interconversion of Nuclear Spin Isomers. *J. Am. Chem. Soc.* **2010**, *132*, 4042–4043.

(96) Li, Y.; Lei, X.; Lawler, R. G.; Murata, Y.; Komatsu, K.; Turro, N. J. Distance-dependent Paramagnet-enhanced Nuclear Spin Relaxation of H<sub>2</sub>@C<sub>60</sub> Derivatives Covalently Linked to a Nitroxide Radical. *J. Phys. Chem. Lett.* **2010**, *1*, 2135–2138.

(97) Sartori, E.; Ruzzi, M.; Lawler, R. G.; Turro, N. J. Nitroxide Paramagnet-induced Para-ortho Conversion and Nuclear Spin Relaxation of H<sub>2</sub> in Organic Solvents. *J. Am. Chem. Soc.* **2008**, *130*, 12752–12756.

(98) Keana, J. F. W.; Pou, S.; Rosen, G. M. Nitroxides as Potential Contrast Enhancing Agent for MRI Application: Influence of Structure on the Rate of Reduction by Rat Hepatocytes, Whole Liver Homogenate, Subcellular Fractions, and Ascorbate. *Magn. Reson. Med.* **1987**, *5*, 525–536.

(99) Bobko, A. A.; Kirilyuk, I. A.; Grigor'ev, I. A.; Zweier, J. L.; Khramtsov, V. V. Reversible Reduction of Nitroxides to Hydroxylamines: Role for Ascorbate and Glutathione. *Free Radical Biol. Med.* **2007**, *42*, 404–412.

(100) Blinco, J. P.; Fairfull-Smith, K. E.; Morrow, B. J.; Bottle, S. E. Profluorescent Nitroxides as Sensitive Probes of Oxidative Change and Free Radical Reactions. *Aust. J. Chem.* **2011**, *64*, 373–389.

(101) Yang, Y.; Zhao, Q.; Feng, W.; Li, F. Luminescent Chemosensors for Bioimaging. *Chem. Rev.* **2013**, *113*, 192–270.

(102) Ahn, H.-Y.; Fairfull-Smith, K. E.; Morrow, B. J.; Lussini, V.; Kim, B.; Bondar, M. V.; Bottle, S. E.; Belfield, K. D. Two-photon Fluorescence Microscopy Imaging of Cellular Oxidative Stress Using Profluorescent Nitroxides. *J. Am. Chem. Soc.* **2012**, *134*, 4721–4730.

(103) Workman, P.; Aboagye, E. O.; Balkwill, F.; Balmain, A.; Bruder, G.; Chaplin, D. J.; Double, J. A.; Everitt, J.; Farningham, D. A. H.; Glennie, M. J.; Kelland, L. R.; Robinson, V.; Stratford, I. J.; Tozer, G. M.; Watson, S.; Wedge, S. R.; Eccles, S. A. Guidelines for the Welfare and Use of Animals in Cancer Research. *Br. J. Cancer* **2010**, *102*, 1555–1577.

(104) Chapman, K.; Sewell, F.; Allais, L.; Delongea, J.-L.; Donald, E.; Festag, M.; Kervyn, S.; Ockert, D.; Nogue, V.; Palmer, H.; Popovic, M.; Roosen, W.; Schoenmakers, A.; Somers, K.; Stark, C.; Stei, P.; Robinson, S. A Global Pharmaceutical Company Initiative: an Evidence-based Approach to Define the Upper Limit of Body Weight Loss in Short Term Toxicity Studies. *Regul. Toxicol. Pharmacol.* **2013**, *67*, 27–38.

(105) Rowland, M.; Benet, L. Z.; Graham, G. G. Clearance Concepts in Pharmacokinetics. *J. Pharmacokinet. Biopharm.* **1973**, *1*, 123–136.